

# Camouflaged Object Detection via Context-aware Cross-level Fusion

Geng Chen\*, Si-Jie Liu\*, Yu-Jia Sun, Ge-Peng Ji, Ya-Feng Wu, Tao Zhou, *Member, IEEE*

**Abstract**—Camouflaged object detection (COD) aims to identify the objects that conceal themselves in natural scenes. Accurate COD suffers from a number of challenges associated with low boundary contrast and the large variation of object appearances, *e.g.*, object size and shape. To address these challenges, we propose a novel Context-aware Cross-level Fusion Network (C<sup>2</sup>F-Net), which fuses context-aware cross-level features for accurately identifying camouflaged objects. Specifically, we compute informative attention coefficients from multi-level features with our Attention-induced Cross-level Fusion Module (ACFM), which further integrates the features under the guidance of attention coefficients. We then propose a Dual-branch Global Context Module (DGCM) to refine the fused features for informative feature representations by exploiting rich global context information. Multiple ACFMs and DGCMs are integrated in a cascaded manner for generating a coarse prediction from high-level features. The coarse prediction acts as an attention map to refine the low-level features before passing them to our Camouflage Inference Module (CIM) to generate the final prediction. We perform extensive experiments on three widely used benchmark datasets and compare C<sup>2</sup>F-Net with state-of-the-art (SOTA) models. The results show that C<sup>2</sup>F-Net is an effective COD model and outperforms SOTA models remarkably. Further, an evaluation on polyp segmentation datasets demonstrates the promising potentials of our C<sup>2</sup>F-Net in COD downstream applications. Our code is publicly available at: <https://github.com/Ben57882/C2FNet-TSCVT>.

**Index Terms**—Camouflaged Object Detection, Context-aware Deep Learning, Feature Fusion, Polyp Segmentation.

## I. INTRODUCTION

OVER the course of evolution, wild animals have developed extensive camouflage abilities in order to survive. In practice, they try to alter their appearance to “perfectly” blend in with their surroundings in order to avoid attracting the notice of other creatures. Recently, camouflage has attracted

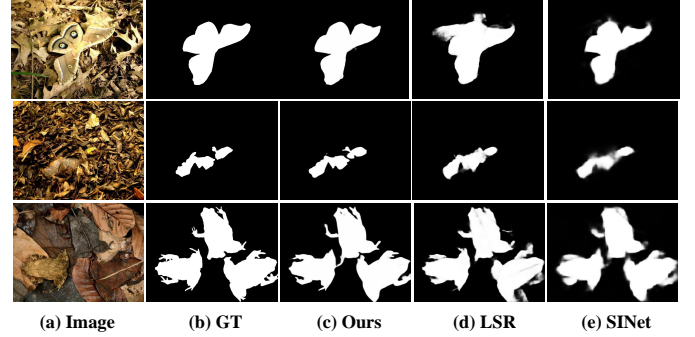


Fig. 1. We show three challenging camouflage scenarios (top to bottom) with indefinable boundary, occluded object, and multiple objects. Our model outperforms cutting-edge models, SINet [15] and LSR [40], in these challenging scenarios.

increasing research interest from the computer vision community [3], [15], [34]. Among various topics, camouflaged object detection (COD), which aims to identify and segment camouflaged objects from images, is particularly popular. However, accurate COD is with considerable difficulties due to the special characteristics of camouflage. More specifically, due to the camouflage, the boundary contrast between an object and its surroundings is extremely low, leading to significant difficulties to identify/segment this object. As shown in the top row of Fig. 1, it is very challenging to discover the butterfly from the leaves. Also, in the middle row of Fig. 1, it is a tremendous task to find out the tortoise occluded by leaves on the ground. In addition, the camouflaged objects, most wild animals, are usually with varied appearances, *e.g.*, size and shape, which further aggravates the difficulties in accurate COD.

To tackle these challenges, deep learning techniques [69] have been adopted and shown great potential. In addition, a number of COD datasets have been constructed for training the deep learning models. For instance, Le *et al.* [34] created the first COD dataset, called CAMO, consisting of 2,500 images. However, CAMO, which suffers from a limited sample size, is insufficient for taking full advantage of deep learning models. Recently, Fan *et al.* [15] constructed COD10K, the first large-scale COD dataset consisting of 10,000 images with the consideration of various challenging camouflage attributes in real natural environments. In addition to datasets, these two works also contribute to the COD from the aspect of deep learning models. Le *et al.* [34] proposed an anabranch network, which classifies whether an image contains camouflaged objects and then integrates this information into the COD task. Motivated

G. Chen, S.-J. Liu, and Y.-F. Wu are with Northwestern Polytechnical University, Xi'an 710072, China. G. Chen is also with National Engineering Laboratory for Integrated Aero-Space-Ground-Ocean Big Data Application Technology, School of Computer Science and Engineering, S.-J. Liu and Y.-F. Wu are also with Data Processing Center, School of Power and Energy (Emails: geng.chen.cs@gmail.com; sijieliu\_123@sina.com; yfwu@nwpu.edu.cn).

T. Zhou is with Key Laboratory of System Control and Information Processing, Ministry of Education, Shanghai 200240, China, and School of Computer Science and Engineering, Nanjing University of Science and Technology, Nanjing 210094, China (Email: taozhou.ai@gmail.com).

Y.-J. Sun is with School of Computer Science, Inner Mongolia University, Hohhot 010021, China (Email: thograce@163.com).

G.-P. Ji is with Artificial Intelligence Institute, School of Computer Science, Wuhan University, Wuhan 430072, China (Email: gepengai.ji@gmail.com).

Equal contribution: Geng Chen and Sijie Liu.

Corresponding authors: Tao Zhou and Yafeng Wu.

Copyright © 2022 IEEE. Personal use of this material is permitted. However, permission to use this material for any other purposes must be obtained from the IEEE by sending an email to [pubs-permissions@ieee.org](mailto:pubs-permissions@ieee.org).

by the fact that predators discover preys by searching first and then recognizing, Fan *et al.* [15] designed searching modules to identify the rough areas of camouflaged objects and then accurately segmented camouflaged objects with identification modules.

Although existing methods have shown promising performance in the detection of a single camouflaged object from relatively simple scenes, their performance degrades for a number of challenging cases, *e.g.*, occlusion, multiple objects, etc. As shown in the top two rows of Fig. 1, state-of-the-art models show unsatisfactory performance when occlusion exists or the boundary of a camouflaged object is indefinable. In addition, they are unable to accurately identify the boundaries of camouflaged objects when multiple camouflaged objects exist, as shown in the bottom row of Fig. 1. These challenges can be addressed with a significantly large receptive field, which provides rich context information for accurate COD. In addition, how to effectively fuse cross-level features also plays a crucial role in the success of COD. However, existing works usually overlook the importance of both of these two key factors. It is, therefore, greatly desired for a unified COD framework that jointly considers rich context information and effective cross-level feature fusion.

To this end, we propose Context-aware Cross-level Fusion Network (C<sup>2</sup>F-Net), a novel deep learning model for accurate COD. In C<sup>2</sup>F-Net, the cross-level features extracted from the backbone are first fused with an attention-induced cross-level fusion module (ACFM), which achieves the feature integration with the clues from a multi-scale channel attention (MSCA) component. More specifically, the ACFM involves three major steps, including (i) attention coefficient computation from multi-level features, (ii) feature refinement with the attention coefficients, and (iii) feature integration for the fused one. Subsequently, a dual-branch global context module (DGCM) is proposed to exploit the rich context information from the fused features. The DGCM transforms the input features into multi-scaled ones with two parallel branches, employs the MSCA components to compute the attention coefficients, and integrates the features under the guidance of the attention coefficients. Multiple ACFMs and DGCMs are organized in a cascaded manner at two stages, from high-level to low-level. The final DGCM predicts a coarse segmentation map of the camouflaged object(s). We then refine the low-level features with the obtained coarse map and perform the final detection with the proposed Camouflage Inference Module (CIM). In summary, our contributions are as follows:

- We propose C<sup>2</sup>F-Net, a novel COD model that integrates the cross-level features by considering rich global context information, effective cross-level fusion, and low-level feature refinement.
- We propose DGCM, a context-aware module that can capture valuable context information for improving the accuracy of COD. Furthermore, we integrate the cross-level features with ACFM, a novel fusion module that integrates the features with the valuable attention cues provided by MSCA.
- We propose CIM, an effective module capable of exploiting informative features from the low-level features

refined by a coarse prediction map.

- Extensive experiments on three benchmark datasets demonstrate that our C<sup>2</sup>F-Net outperforms 19 state-of-the-art models in the terms of five evaluation metrics for the COD task. Further poly segmentation experiments indicate the superior performance of our C<sup>2</sup>F-Net in COD downstream applications.

This paper significantly extends our previous work published in the IJCAI 2021 [52], with multi-fold improvements as follows. (i) We improve the model by refining the low-level features with the coarse COD map and then predicting the final result with our CIM. The new improvement is detailed in Sec. III-D and has shown promising performance in both quantitative and qualitative evaluations (see Sec. IV). (ii) We provide more details to the conference version. Specifically, we add a subsection to review the downstream applications of COD and present recent advances in poly segmentation (see Sec. II-C). We also provide the details of evaluation metrics to better understand their characteristics (see Sec. IV-C). (iii) We compare the proposed model with more state-of-the-art methods to validate the effectiveness of our model (see Sec. IV-D), and provide a sub-class comparison and a more insightful discussion (see Sec. IV-D2). (iv) We extend the proposed C<sup>2</sup>F-Net to a downstream application of COD, *i.e.*, polyp segmentation. Quantitative and qualitative evaluations conducted on four benchmark datasets demonstrate the superiority of our model over other existing polyp segmentation methods (see Sec. IV-F).

The rest of this paper is arranged as follows. In Section II, we review a number of works that are closely related to ours. In Section III, we describe our C<sup>2</sup>F-Net in detail. In Section IV, we provide extensive experimental results, ablation studies, and the further application of our C<sup>2</sup>F-Net in polyp segmentation. Finally, we conclude this work in Section V.

## II. RELATED WORK

In this section, we discuss three types of works that are closely related to our method, *i.e.*, camouflaged object detection, context-aware deep learning, and downstream applications of COD.

### A. Camouflaged Object Detection

Recently, significant efforts have been put into COD, which is an emerging field in the computer vision community. Early COD approaches identify camouflaged objects with visual features, including texture, color, gradient, and motion [44]. In practice, a single visual feature cannot provide comprehensive characteristics for camouflaged objects. Therefore, multiple features are integrated for improving performance [32]. Moreover, the Bayesian framework has been employed for detecting moving camouflaged objects from videos [64]. Despite their advantages, existing approaches relying on hand-crafted features tend to fail in real-world applications since they can only work with relatively simple scenarios. To this end, deep learning models, which automatically learn features and are trained in an end-to-end manner, have been adopted for accurate COD, which acts as an effective solution to

address the challenges associated with traditional hand-crafted features. Yan *et al.* [60] proposed a two-stream network, called MirrorNet, for COD with the original and flipped images. The underlying motivation lies in the fact that the flipped image can provide valuable cues for COD. Lamdouar *et al.* [33] identified camouflaged objects from videos by exploiting the motion information with a deep learning framework, which consists of two modules, *i.e.*, a differentiable registration module and a motion segmentation module. Ren *et al.* [47] proposed a two-step texture-aware refinement module to amplify the differences between the camouflaged object and its surroundings for accurate COD. Ji *et al.* [31] designed a multivariate calibration strategy to contrast the initial edge prior obtained from a selective edge aggregation strategy that mimics human visual perception. Li *et al.* [35] presented an adversarial learning network with a similarity measure module to model the contradictory information, enhancing the ability to detect salient and camouflaged objects. Mei *et al.* [43] developed a bio-inspired framework named Positioning and Focus Network, which contains a positioning module for mimicking the detection process of predator and a focus module to perform the identification process. Lyu *et al.* [40] proposed the first ranking-based network based on Mask-RCNN [24] to learn the camouflage degree with joint fixation and camouflage decoder. They also collect the large-scale testing dataset NC4K. SINetV2 [16] designed a neighbor connection decoder and group-reversal attention for detecting camouflaged objects. Interested readers can refer to [3] for a comprehensive review of COD. Furthermore, it is worth noting that COD shares a number of similarities with the popular salient object detection (SOD) tasks, such as RGB SOD [66], RGB-Depth/RGB-Thermal SOD [7], [25], [62], remote sensing SOD [10], [63], Co-SOD [9], [18], etc. Different from existing models, our C<sup>2</sup>F-Net advances the COD accuracy by jointly considering the rich global context information, effective cross-level fusion, and low-level feature refinement.

### B. Context-aware Deep Learning

Due to its superior capability of enhancing the feature representation, contextual information acts as a vital role in segmenting objects. For this reason, efforts have been made to enrich the contextual information. For instance, Zhao *et al.* [65] proposed PSPNet to establish multi-scale representations around each pixel for obtaining rich context information. Chen *et al.* [6] constructed ASPP with different dilated convolutions in order to enrich context information. The self-attention mechanism has also been proposed and employed for capturing rich context information. Typical instances include DANet [22], which extracts contextual information with non-local modules [56], and CCNet [27], which employs multiple cascaded cross-attention modules to obtain dense contextual information. Context information also gains significant attention from the field of object segmentation. For instance, Zhang *et al.* [61] enriched context information with a multi-scale context-aware feature extraction module, which provides rich context information. Liu *et al.* [38] proposed PoolNet, which is equipped with a pyramid pool module for rich context features

highly related to the accurate salient object detection. Chen *et al.* [8] proposed a global context flow module to transfer features containing global semantic information to multi-level features at different stages to improve the integrity of SOD. Tan *et al.* [54] integrated the local and global context features in an adaptive coarse-to-fine manner for improved feature representations. Besides, the motion context and information have been effectively exploited and used in motion prediction [50] and activity recognition [49].

### C. Downstream Applications of COD

COD has a large number of downstream applications in practice. Typical instances include medical image segmentation (*e.g.*, polyp segmentation [29], [30], COVID-19 lung infection segmentation [20], *etc.*), surface defect detection, recreational art, concealed-salient object transition, transparent objects detection, search engines, *etc* [16].

Among various applications, polyp segmentation is one of the most attractive tasks due to its vital application value and close relationship with COD. Accurate polyp segmentation can provide vital information from colonoscopy images for identifying polyps, which have a high risk to develop into serious colorectal cancer that threatens human life. Early polyp segmentation methods rely on hand-crafted features [41], which are unable to fully capture the useful information for segmenting polyps. To address these challenges, deep learning has been employed for polyp segmentation and has shown great success. For instance, Brandao *et al.* [4] utilized the fully convolutional networks (FCNs) to segment polyps in an end-to-end manner. Akbari *et al.* [1] employed modified FCNs for accurate polyp segmentation. The variants of U-Net, *i.e.*, U-Net++ [68] and ResUNet++ [28], were also utilized for polyp segmentation for improved performance. Boundary information was also employed for improving the accuracy of polyp segmentation [21], [45]. Ji *et al.* [29] proposed a normalized self-attention module to progressively segment the polyp region in the video clips. More recently, Fan *et al.* [17] proposed PraNet to segment polyps with paralleled partial decoder and reverse attention mechanism, significantly improving the performance. In this study, we further demonstrate the effectiveness of our C<sup>2</sup>F-Net by applying it to the polyp segmentation task.

## III. PROPOSED METHOD

In this section, we first present the overall framework of the proposed C<sup>2</sup>F-Net. Then, we detail three key components in our C<sup>2</sup>F-Net. Finally, we detail the overall loss function for the proposed COD method.

### A. Overall Architecture

Fig. 2 shows the overall framework of our C<sup>2</sup>F-Net, which can effectively integrate context-aware cross-level features to boost the accuracy of camouflaged object detection. Specifically, Res2Net-50 [23] is adopted as the backbone to extract multi-scale features, denoted as  $f_i$  with  $i = 1, 2, \dots, 5$ . In our model, the extracted features are divided into two groups, *i.e.*,

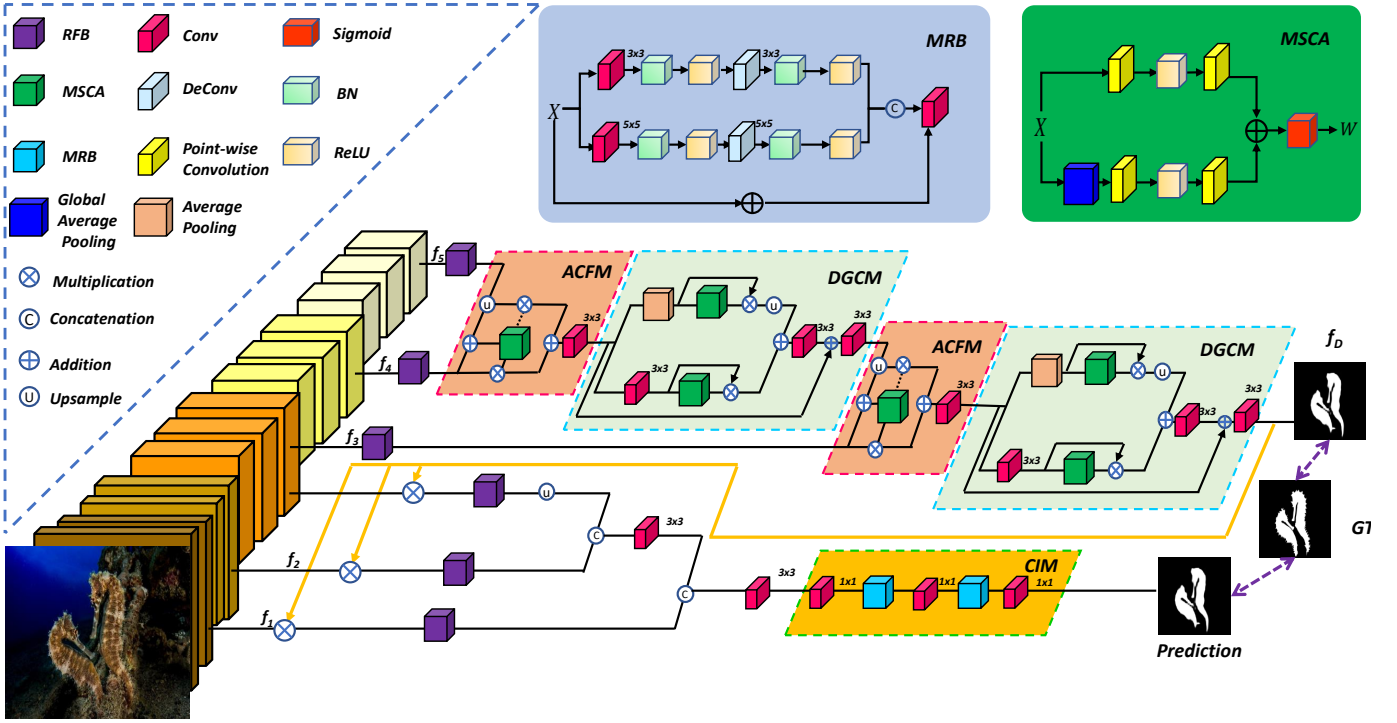


Fig. 2. The overall framework of our C<sup>2</sup>F-Net, including three main components, *i.e.*, attention-induced cross-level fusion module (ACFM), dual-branch global context module (DGCM), and camouflage inference module (CIM). Note that MRB and MSCA are short names for multi-scale residual block and multi-scale channel attention, respectively. See Sec. III for details.

low-level features  $Q_l = \{f_1, f_2, f_3\}$  and high-level features  $Q_h = \{f_3, f_4, f_5\}$ . Then, three receptive field blocks (RFB) are utilized to enrich the features from  $Q_h$  by expanding the receptive fields. We utilize the same setting in [23], and the RFB includes five branches  $b_k$  with  $k = 1, 2, \dots, 5$ . In each branch, a  $1 \times 1$  convolutional layer is first adopted to reduce the original channel size to 64. Following that, a  $(2k-1) \times (2k-1)$  convolutional layer and a  $3 \times 3$  convolutional layer with a specific dilation rate  $(2k-1)$  (when  $k > 2$ ) are adopted. The first four branches are concatenated to obtain the fused feature, which is fed into a  $1 \times 1$  convolutional layer for reducing the channel size to 64. Besides, the output of the fifth branch is added by the feature from the first four branches, which is further fed to a  $ReLU$  activation to obtain the final feature. Moreover, an attention-induced cross-level fusion module (ACFM) is proposed to fuse high-level features, and a dual-branch global context module (DGCM) is proposed to fully exploit multi-scale context information from the fused features. Two modules are organized in a cascaded manner. The last DGCM provides an initial prediction  $f_D$ . We then refine the low-level features  $Q_l$  with  $f_D$  and predict the final COD result with our camouflage inference module (CIM).

### B. Attention-induced Cross-level Fusion Module

Natural differences often exist among different types of camouflaged objects. What's more, due to the observation distance and relative locations to the surrounding background, the size of similar camouflaged objects could change dramatically. To address the above issues, we design a novel ACFM by introducing a multi-scale channel attention (MSCA) [11]

strategy to integrate cross-level features, which can effectively mine multi-scale information to alleviate scale variations.

The detailed structure of MSCA is shown in Fig. 2. In MSCA, it is a self-attention based on a two-branch structure. Specifically, the first branch adopts global average pooling (GAP) to exploit global contexts, which can emphasize globally distributed for large objects. The second branch holds the size of the original feature to obtain local contexts, which can prevent small camouflaged objects that are often ignored. Different from several existing multi-scale attention mechanisms, MSCA adopts point convolution in two branches to restore and compress features along the channel dimension, resulting in aggregating multi-scale context information. Cross-level features have different contributions to the COD task, thus fusing multi-level features can complement each other to obtain more comprehensive feature representations. To achieve this, we conduct ACFM on high-level features, and the cross-level fusion process is implemented by

$$F_{ab} = \mathcal{M}(F_a \uplus F_b) \otimes F_a \oplus (1 - \mathcal{M}(F_a \uplus F_b)) \otimes F_b, \quad (1)$$

where  $\mathcal{M}$  denotes the MSCA operation,  $F_a$  and  $F_b$  denote the two input features. Besides,  $\oplus$  denotes the initial fusion of  $F_a$  and  $F_b$ , in which  $F_b$  is up-sampled and then added with  $F_a$ .  $\otimes$  denotes element-wise multiplication.  $(1 - \mathcal{M}(F_a \uplus F_b))$  corresponds to the dotted line in Fig. 2. Moreover,  $F_{ab}$  is then fed into a  $3 \times 3$  convolutional layer, followed by batch normalization and a  $ReLU$  function. Thus, we can obtain the fused cross-level feature, *i.e.*,  $F$ .

### C. Dual-branch Global Context Module

The proposed ACFM is adopted to fuse multi-scale features, in which a multi-scale channel attention strategy is introduced to obtain informative attention-based features. In addition, global context information is important for boosting the COD performance. Thus, a dual-branch global context module (DGCM) is proposed to fully mine global context information from the fused features. In detail, the output  $F \in \mathbb{R}^{W \times H \times C}$  of the ACFM is first fed to two branches with a convolutional layer and average pooling, respectively, thus we obtain the sub-features  $F_c \in \mathbb{R}^{W \times H \times C}$  and  $F_p \in \mathbb{R}^{\frac{W}{2} \times \frac{H}{2} \times C}$ . After that, in order to learn multi-scale attention-based features,  $F_c$  and  $F_p$  are also fed to the MSCA module. Then, an element-wise multiplication is utilized to integrate the feature outputs of MSCA and the corresponding features ( $F_c$  or  $F_p$ ), and then we obtain  $F_{cm} \in \mathbb{R}^{W \times H \times C}$  and  $F_{pm} \in \mathbb{R}^{\frac{W}{2} \times \frac{H}{2} \times C}$ . Further, we adopt an addition operation to integrate the features from the above two-branch structure, and then the fused feature is denoted as  $F_{cpm}$ . Finally, the residual connection is adopted to combine  $F$  with  $F_{cpm}$  to obtain  $F'$ . The detailed processing steps are presented as follows:

$$\begin{cases} F_c = \mathcal{C}(F), F_{cm} = F_c \otimes \mathcal{M}(F_c), \\ F_p = \mathcal{C}(\mathcal{P}(F)), F_{pm} = F_p \otimes \mathcal{M}(F_p), \\ F' = \mathcal{C}(F \oplus \mathcal{C}(F_{cm} \oplus \mathcal{U}(F_{pm}))), \end{cases} \quad (2)$$

where  $\mathcal{C}$ ,  $\mathcal{M}$ ,  $\mathcal{P}$ , and  $\mathcal{U}$  denote the convolution, MSCA, average pooling, and upsampling operation, respectively.

**Remarks.** It is worth noting that our DGCM aims to enhance the fused features of ACFM, so that the proposed model adaptively extracts multi-scale information from a specific level. For clarity, the overall structure is presented in Fig. 2.

### D. Camouflage Inference Module

To effectively make use of multi-scale features, the low-level features (*i.e.*,  $Q_l = \{f_1, f_2, f_3\}$ ) are refined by using the output (denoted as  $f_D$ ) of the second DGCM. The refinement flow is presented to effectively fuse all the features from multiple layers. Followed the setting in the BBS-Net [19], we utilize a modified RFB module (denoted as  $\mathcal{R}$ ) to fully expand the receptive fields for obtaining richer features and reducing the computation. As shown in Fig. 2,  $f_D$  is adopted to refine three low-level features by using an element-wise multiplication operation, *i.e.*,  $f_1 \otimes f_D$ ,  $f_2 \otimes f_D$ , and  $f_3 \otimes f_D$ . Each refined feature is fed into a RFB module, and we can obtain  $\mathcal{R}(f_1 \otimes f_D)$ ,  $\mathcal{R}(f_2 \otimes f_D)$ , and  $\mathcal{R}(f_3 \otimes f_D)$ . Then,  $\mathcal{R}(f_1 \otimes f_D)$  and  $\mathcal{R}(f_2 \otimes f_D)$  are cascaded and fed into a Conv block. After that, the output and  $\mathcal{R}(f_3 \otimes f_D)$  are further cascaded and fed into a Conv block with a channel size of 16.

Further, we propose a Camouflage Inference Module (CIM) to generate the final detection results, which can take advantage of the low-level features via a multi-scale strategy. In the CIM, to fully exploit multi-scale information, we further propose a Multi-scale Residual Block (MRB) to detect local and multi-scale features. Specifically, we build a two-stream network and each stream utilizes a different convolutional kernel. As shown in Fig. 2, the current feature representation  $X$  is fed to the first stream network with two sequential

operations, in which the former sequential operation consists of a  $3 \times 3$  convolution followed by batch normalization and a *ReLU* function (denoted “ $B_{conv3}$ ”), and the latter consists of a  $3 \times 3$  transpose convolution followed by batch normalization and a *ReLU* function (denoted “ $B_{Dconv3}$ ”). Besides,  $X$  is also fed to the second stream network two other sequential operations, in which the convolutional kernel is  $5 \times 5$ . The above processing steps can be presented as follows:

$$\begin{cases} F_{conv3} = B_{Dconv3 \times 3}(B_{conv3 \times 3}(X)), \\ F_{conv5} = B_{Dconv5 \times 5}(B_{conv5 \times 5}(X)). \end{cases} \quad (3)$$

Then, the stream features are cascaded and then fed into a  $3 \times 3$  sequential layer to obtain the fused multi-scale feature representation, *i.e.*,  $F_f = B_{conv3 \times 3}(\text{Cat}(F_{conv3}, F_{conv5}))$ . To preserve the original information from the input  $X$ , we adopt residual learning in the MRB. Therefore, we obtain the output of each MRB by adding  $X$  and the fused multi-scale feature. The whole CIM consists of three  $1 \times 1$  convolution and two MRB, which is used to generate the final prediction  $P$ .

### E. Loss Function

The binary-cross entropy loss ( $\mathcal{L}_{\text{BCE}}$ ) is widely used to calculate the loss of each pixel to form a pixel restriction on the network. To effectively exploit the global structure, the work [46] introduced IoU loss ( $\mathcal{L}_{\text{IoU}}$ ) to form a global restriction on the network. However, the above losses are often treated equally to all pixels, ignoring the differences among pixels. To overcome this issue, this work [57] improves  $\mathcal{L}_{\text{BCE}}$  and  $\mathcal{L}_{\text{IoU}}$  into the weighted binary cross-entropy loss ( $\mathcal{L}_{\text{BCE}}^w$ ) and IoU loss ( $\mathcal{L}_{\text{IoU}}^w$ ). Specifically, by computing the difference between the center pixel and its surroundings, each pixel can be assigned a different weight, so that the hard pixels are paid more attention. In this case, the basic loss function of the proposed model is defined as:  $\mathcal{L} = \mathcal{L}_{\text{IoU}}^w + \mathcal{L}_{\text{BCE}}^w$ . To further achieve the aim of joint optimization, the total loss of our model can be defined by

$$\mathcal{L} = \mathcal{L}(f_D, G) + \mathcal{L}(P, G), \quad (4)$$

where  $\mathcal{L}(f_D, G)$  denotes the loss between the initial prediction map and ground truth, and  $\mathcal{L}(P, G)$  denotes the loss between the final prediction map and ground truth.

## IV. EXPERIMENTS

In this section, we first present the implementation details, datasets, and evaluation metrics used in our experiments. Then, we show quantitative and qualitative results by comparing our model with other existing methods. Further, we conduct ablation studies to validate the effectiveness of each key component. Finally, we extend the application of our model to polyp segmentation.

### A. Implementation Details

The proposed model is implemented using PyTorch, and the Res2Net-50 [23] pretrained on ImageNet is adopted as the backbone. We adopt the AdaX [36] algorithm to optimize the overall framework. To enhance the generalizability of

TABLE I

QUANTITATIVE COMPARISON BETWEEN OUR MODEL AND OTHER STATE-OF-THE-ART COD METHODS ON THREE DATASETS IN TERMS OF FIVE METRICS (i.e.,  $S_\alpha$ ,  $E_\phi$ ,  $F_\beta^w$ ,  $F_\beta$  AND  $M$ ). “↓” / “↑” INDICATES THAT SMALLER OR LARGER IS BETTER. BEST RESULTS ARE HIGHLIGHTED IN **BOLD**.

Method	Year	Backbone	CAMO-Test					CHAMELEON					COD10K-Test				
			$S_\alpha \uparrow$	$E_\phi \uparrow$	$F_\beta^w \uparrow$	$F_\beta \uparrow$	$M \downarrow$	$S_\alpha \uparrow$	$E_\phi \uparrow$	$F_\beta^w \uparrow$	$F_\beta \uparrow$	$M \downarrow$	$S_\alpha \uparrow$	$E_\phi \uparrow$	$F_\beta^w \uparrow$	$F_\beta \uparrow$	$M \downarrow$
FPN [37]	2017	ResNet-50	0.684	0.791	0.483	0.642	0.131	0.794	0.835	0.590	0.676	0.075	0.697	0.711	0.411	0.484	0.075
MaskRCNN [24]	2017	ResNet-50	0.574	0.716	0.43	0.521	0.151	0.643	0.780	0.512	0.612	0.099	0.613	0.750	0.402	0.470	0.080
PSPNet [65]	2017	ResNet-50	0.663	0.778	0.445	0.605	0.139	0.773	0.814	0.555	0.650	0.085	0.678	0.688	0.377	0.451	0.080
PiCANet [39]	2018	ResNet-50	0.609	0.753	0.356	0.538	0.155	0.769	0.836	0.536	0.668	0.084	0.649	0.678	0.322	0.423	0.083
UNet++ [68]	2018	VGGNet-16	0.599	0.740	0.392	0.522	0.149	0.695	0.808	0.501	0.586	0.094	0.623	0.718	0.350	0.431	0.086
BASNet [46]	2019	ResNet-34	0.618	0.713	0.413	0.525	0.159	0.688	0.742	0.474	0.546	0.118	0.634	0.676	0.365	0.421	0.105
CPD [59]	2019	ResNet-50	0.716	0.807	0.556	0.675	0.113	0.857	0.898	0.731	0.775	0.048	0.750	0.792	0.531	0.578	0.053
HTC [5]	2019	ResNet-50	0.477	0.442	0.174	0.338	0.172	0.517	0.490	0.204	0.327	0.129	0.548	0.521	0.221	0.298	0.088
MSRCNN [26]	2019	ResNet-50	0.618	0.670	0.454	0.544	0.133	0.637	0.688	0.443	0.529	0.091	0.641	0.708	0.419	0.486	0.073
PoolNet [38]	2019	ResNet-50	0.703	0.790	0.494	0.628	0.128	0.776	0.824	0.555	0.649	0.078	0.705	0.708	0.416	0.479	0.070
EGNet [66]	2019	ResNet-50	0.662	0.780	0.495	0.640	0.125	0.750	0.854	0.531	0.694	0.075	0.733	0.799	0.519	0.572	0.055
ANet-SRM [34]	2019	FCN	0.682	0.725	0.484	0.593	0.126	‡	‡	‡	‡	‡	‡	‡	‡	‡	‡
SINet [15]	2020	ResNet-50	0.752	0.835	0.606	0.709	0.100	0.868	0.899	0.740	0.776	0.044	0.771	0.797	0.551	0.593	0.051
MirrorNet [60]	2020	ResNet-50	0.784	0.849	0.652	0.767	0.078	‡	‡	‡	‡	‡	‡	‡	‡	‡	‡
UCNet [58]	2020	ResNet-50	0.739	0.811	0.640	0.716	0.094	0.880	0.929	0.817	0.830	0.036	0.776	0.867	0.633	0.673	0.042
PraNet [17]	2020	Res2Net-50	0.769	0.833	0.663	0.715	0.094	0.860	0.898	0.763	0.775	0.044	0.789	0.839	0.629	0.640	0.045
LSR [40]	2021	ResNet-50	0.787	0.855	0.696	0.756	0.080	0.890	0.936	0.822	0.835	0.030	0.804	0.882	0.673	0.699	0.037
PFNet [43]	2021	ResNet-50	0.782	0.852	0.695	0.751	0.085	0.882	0.942	0.816	0.820	0.033	0.800	0.868	0.660	0.676	0.040
ERRNet [31]	2022	ResNet-50	0.779	0.851	0.679	0.731	0.085	0.868	0.917	0.787	0.796	0.039	0.786	0.845	0.630	0.646	0.043
C <sup>2</sup> F-Net	2022	ResNet-50	0.765	0.838	0.680	0.732	0.087	0.878	0.938	0.822	0.846	0.031	0.776	0.872	0.640	0.688	0.042
	2022	Res2Net-50	<b>0.800</b>	<b>0.869</b>	<b>0.730</b>	<b>0.777</b>	<b>0.077</b>	<b>0.893</b>	<b>0.947</b>	<b>0.845</b>	<b>0.836</b>	<b>0.028</b>	<b>0.811</b>	<b>0.891</b>	<b>0.691</b>	<b>0.718</b>	<b>0.036</b>

the proposed model, we adopt a multi-scale training strategy  $\{0.75, 1, 1.25\}$  in the training stage. Besides, the input images are resized to  $352 \times 352$ . The initial learning rate is set to  $1e-4$ , which will decay 10 times after 30 epochs. The network is trained on an NVIDIA Tesla V100 GPU. The batch size is set to be 30, and the training process takes about 6 hours over 100 epochs.

### B. Datasets

To validate the effectiveness of the proposed model, we carry out comparison experiments on three benchmark datasets. The details of each COD dataset are provided below.

- CHAMELEON [15] is collected using the Google search engine with the keyword “camouflage animals”, which consists of 76 camouflaged images using as a testing dataset.
- CAMO [34] consists of 1,250 camouflaged images (1,000 for training, 250 for testing), which includes eight categories.
- COD10K [15] is currently the largest COD dataset with pixel-level annotations. It consists of 5,066 images, where 3,040 for training and 2,026 for testing. Besides, this dataset is split into 5 super-classes and 69 sub-classes.

**Training and testing settings.** Following the setting in [15], for the CAMO dataset, we utilize the default training set. For the COD10K dataset, we utilize the default training camouflaged images. In the test stage, we test our C<sup>2</sup>F-Net and other compared methods on the test sets of CAMO and COD10K, and the whole CHAMELEON dataset.

### C. Evaluation Metrics

We adopt five widely used metrics, namely MAE ( $M$ ), S-measure ( $S_\alpha$ ), F-measure ( $F_\beta$ ), weighted F-measure ( $F_\beta^w$ ), and

E-measure ( $E_\phi$ ), to evaluate the effectiveness of our model and all compared methods. The detailed definitions for these metrics are as follows:

- 1) Mean absolute error (MAE,  $M$ ) computes the average difference between the normalized prediction and ground truth, which is defined by

$$M = \frac{1}{W \cdot H} \sum_{x=1}^W \sum_{y=1}^H |P(x, y) - G(x, y)|, \quad (5)$$

where  $P(x, y)$  and  $G(x, y)$  correspond to the prediction map and ground truth value at the pixel location  $(x, y)$ .  $W$  and  $H$  are the width and height of the prediction map  $P$ .

- 2) S-measure ( $S_\alpha$ ) [12] computes the object-aware similarity  $S_o$  and region-aware structure similarity  $S_r$  between the prediction map and the ground truth by

$$S_\alpha = \alpha * S_o + (1 - \alpha) * S_r, \quad (6)$$

where  $\alpha$  is a trade-off parameter to balance  $S_o$  and  $S_r$ , and it is set to 0.5 as in [12].

- 3) F-measure ( $F_\beta$ ) is employed to evaluate binary map results between the prediction and the ground truth. It is defined as:

$$F_\beta = \frac{(1 + \beta^2) Precision \cdot Recall}{\beta^2 Precision + Recall}, \quad (7)$$

where  $\beta$  is the weight between the precision and recall.  $\beta^2 = 0.3$  is the default setting since the precision is often weighted more than the recall. Besides, the improved version of  $F_\beta$ , i.e., weighted F-measure ( $F_\beta^w$ ), is proposed to overcome the interpolation, dependency,



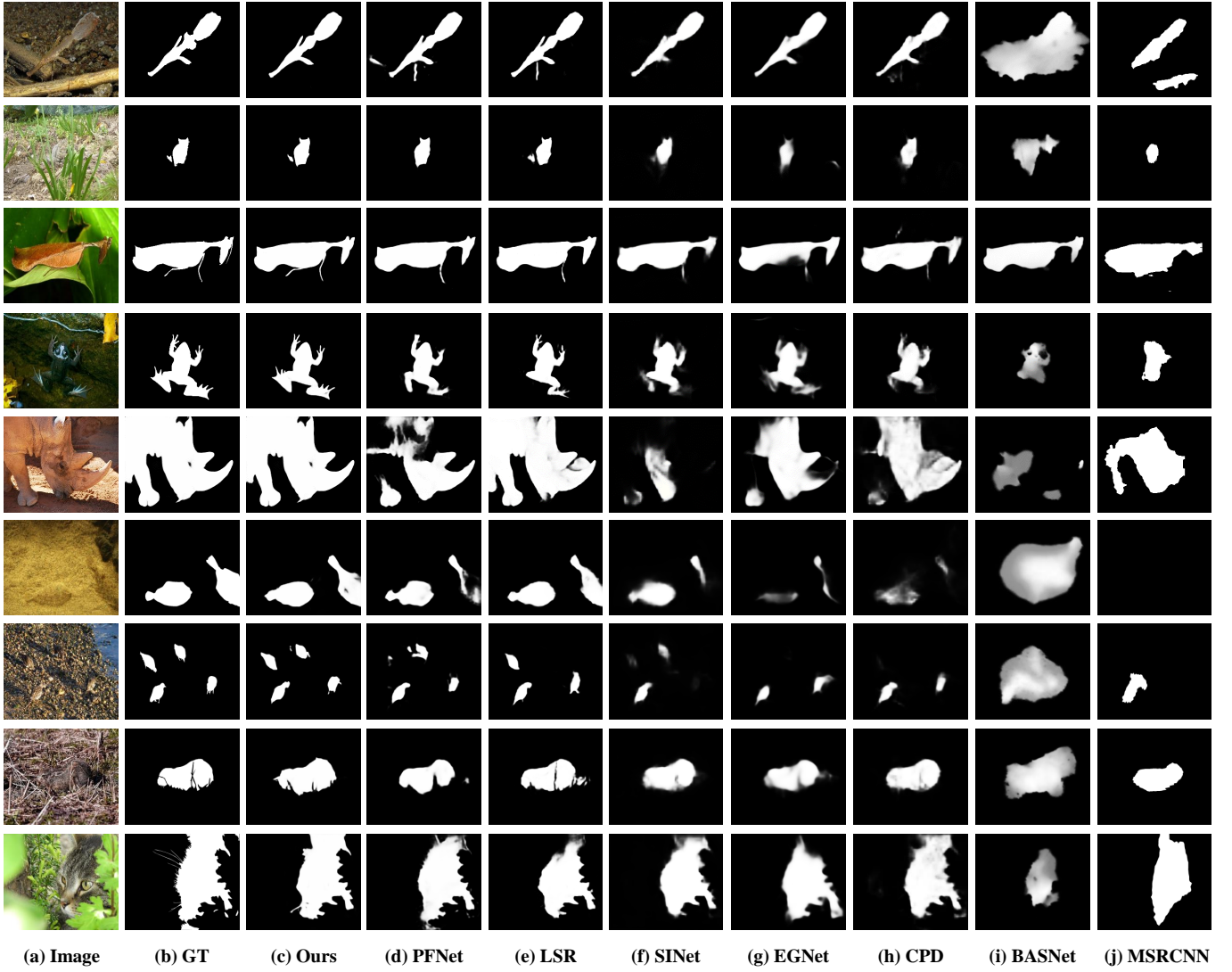


Fig. 3. Qualitative results of our model and seven state-of-the-art COD methods (*i.e.*, PFNet [43], LSR [40], SINet [15], EGNet [66], CPD [59], BASNet [46], and MSRCNN [26]).

and equal-importance flaws of  $F_\beta$ . This metric synthetically considers both weighted precision and weighted recall [42].

- 4) E-measure( $E_\phi$ ) [13], [14] evaluates the overall and local accuracy of a binary foreground map, which can be defined by

$$E_\phi = \frac{1}{W \cdot H} \sum_{x=1}^W \sum_{y=1}^H \phi(x, y). \quad (8)$$

In summary, for these five metrics above, higher  $S_\alpha$ ,  $F_\beta^w$ ,  $F_\beta$ ,  $E_\phi$ , and lower  $M$  indicate better performance. Note that we adopt adaptive F/E-measure in our evaluation.

#### D. Comparison with State-of-the-art COD Methods

We compare the proposed method with 19 state-of-the-art (SOTA) COD methods, including FPN [37], MaskRCNN [24], PSPNet [65], UNet++ [68], PiCANet [39], MSRCNN [26], BASNet [46], PFNet [67], CPD [59], HTC [5], EGNet [66],

ANet-SRM [34], SINet [15], MirrorNet [60], UCNNet [58], PraNet [17], LSR [40], PFNet [43], and ERRNet [31]. For a fair comparison, the results of MirrorNet are collected from link<sup>1</sup>, the results of ERRNet are taken from link<sup>2</sup>, and the results of remaining 18 methods are collected from link<sup>3</sup>.

1) *Quantitative Evaluation*: Table I shows the quantitative results of the proposed model, all compared COD methods on the three benchmark datasets. Meanwhile, the backbones of all the methods are provided in Table I.

**Performance on CAMO.** From Table I, compared with 19 SOTA models, it can be observed that our C<sup>2</sup>F-Net performs better than other models in terms of all metrics. Specifically, compared with LSR, the second-best model,  $S_\alpha$ ,  $F_\beta^w$ , and  $E_\phi$  increased by 1.6%, 4.9%, and 1.6%, respectively. This is mainly because that the proposed ACFM can mine multi-scale information to alleviate scale variations, and DCCM aims

<sup>1</sup><https://sites.google.com/view/ltngghia/research/camo>

<sup>2</sup><https://github.com/GewelsJI/ERRNet>

<sup>3</sup><http://dpfan.net/socbenchmark>

TABLE II

RESULTS COMPARISON BETWEEN OUR MODEL AND OTHER STATE-OF-THE-ART COD METHODS FOR THE COD10K DATASET ON FOUR SUPER-CLASSES IN TERMS OF FOUR EVALUATION METRICS (*i.e.*,  $S_\alpha$ ,  $E_\phi$ ,  $F_\beta$  ↑ AND  $M$ ). “↑” / “↓” INDICATES THAT LARGER OR SMALLER IS BETTER. BEST RESULTS ARE HIGHLIGHTED IN **BOLD FONTS**.

Method	Year	Aquatic				Terrestrial				Flying				Amphibian			
		$S_\alpha$ ↑	$E_\phi$ ↑	$F_\beta$ ↑	$M$ ↓	$S_\alpha$ ↑	$E_\phi$ ↑	$F_\beta$ ↑	$M$ ↓	$S_\alpha$ ↑	$E_\phi$ ↑	$F_\beta$ ↑	$M$ ↓	$S_\alpha$ ↑	$E_\phi$ ↑	$F_\beta$ ↑	$M$ ↓
FPN [37]	2017	0.684	0.730	0.533	0.103	0.669	0.679	0.418	0.071	0.726	0.724	0.500	0.061	0.745	0.772	0.576	0.065
MaskRCNN [24]	2017	0.560	0.721	0.418	0.123	0.608	0.749	0.441	0.070	0.644	0.767	0.520	0.063	0.665	0.785	0.554	0.081
PSPNet [65]	2017	0.659	0.706	0.449	0.111	0.658	0.652	0.391	0.074	0.700	0.703	0.463	0.067	0.736	0.739	0.535	0.072
PiCANet [39]	2018	0.628	0.698	0.466	0.115	0.625	0.640	0.357	0.075	0.677	0.696	0.441	0.069	0.704	0.727	0.521	0.079
UNet++ [68]	2018	0.599	0.708	0.445	0.121	0.593	0.692	0.369	0.081	0.659	0.745	0.470	0.068	0.677	0.754	0.512	0.079
BASNet [46]	2019	0.620	0.678	0.451	0.134	0.601	0.630	0.351	0.109	0.664	0.711	0.454	0.086	0.708	0.739	0.529	0.087
CPD [59]	2019	0.746	0.806	0.624	0.075	0.714	0.757	0.506	0.052	0.777	0.809	0.603	0.041	0.816	0.854	0.676	0.041
HTC [5]	2019	0.507	0.495	0.292	0.129	0.530	0.485	0.236	0.078	0.582	0.559	0.345	0.070	0.606	0.598	0.403	0.088
MSRCNN [26]	2019	0.614	0.686	0.475	0.107	0.610	0.672	0.426	0.070	0.675	0.744	0.529	0.058	0.722	0.786	0.618	0.055
PoolNet [38]	2019	0.689	0.721	0.519	0.099	0.677	0.672	0.417	0.064	0.733	0.725	0.496	0.057	0.767	0.775	0.583	0.059
EGNet [66]	2019	0.693	0.787	0.590	0.088	0.711	0.773	0.513	0.049	0.771	0.828	0.606	0.039	0.787	0.835	0.649	0.048
SINet [15]	2020	0.758	0.806	0.631	0.073	0.743	0.765	0.532	0.050	0.798	0.817	0.614	0.040	0.827	0.847	0.684	0.042
UCNet [58]	2020	0.768	0.853	0.701	0.060	0.742	0.845	0.608	0.042	0.807	0.892	0.705	0.030	0.827	0.916	0.751	0.034
PraNet [17]	2020	0.780	0.832	0.670	0.065	0.756	0.810	0.577	0.046	0.819	0.864	0.668	0.033	0.842	0.892	0.730	0.035
LSR [40]	2021	0.803	0.873	0.727	0.052	0.772	0.858	0.639	<b>0.038</b>	0.830	0.907	0.726	<b>0.026</b>	0.846	<b>0.922</b>	0.774	<b>0.030</b>
PFNet [43]	2021	0.793	0.865	0.706	0.056	0.773	0.850	0.621	0.041	0.824	0.887	0.698	0.030	<b>0.848</b>	0.896	0.753	0.031
ERRNet [31]	2022	0.781	0.846	0.670	0.061	0.753	0.816	0.580	0.045	0.814	0.867	0.676	0.032	0.834	0.885	0.736	0.036
C <sup>2</sup> F-Net	2022	<b>0.810</b>	<b>0.884</b>	<b>0.736</b>	<b>0.049</b>	<b>0.782</b>	<b>0.869</b>	<b>0.665</b>	0.039	<b>0.835</b>	<b>0.915</b>	<b>0.750</b>	<b>0.026</b>	<b>0.848</b>	0.920	<b>0.784</b>	0.031

to enhance the fused features of ACFM for providing global context information. More importantly, the proposed CIM can make use of the low-level features and further exploit multi-scale information to boost the COD performance.

**Performance on CHAMELEON.** Our C<sup>2</sup>F-Net is also tested on CHAMELEON [15] dataset. As reported in Table I, our C<sup>2</sup>F-Net obtains better performances across all the metrics. Specifically, compared with the LSR,  $E_\phi$  and  $F_\beta^w$  increase by 1.2% and 2.7%, respectively. Overall, the results demonstrate the good generalization ability of our model.

**Performance on COD10K.** The COD10K dataset is a more challenging sequence, which contains 2,026 testing images distributed in 5 super-classes. It can be observed that our C<sup>2</sup>F-Net achieves the new SOTA performances across all five metrics. The main reason for this robustness results is that the mature designed modules can combine multi-level features and exploit rich global context information.

2) *Per-subclass Performance:* In addition to the overall quantitative comparison on the COD10K dataset, the super-class results are also presented in Table II. In this experiment, four main super-classes, including “Aquatic”, “Terrestrial”, “Flying”, and “Amphibian”, are taken into consideration. From the results in Table II, it can be seen that C<sup>2</sup>F-Net out-

performs other SOTA methods on the super-class “Aquatic” and “Flying” in terms of all four metrics. On the super-class “Terrestrial”, as shown in Table II, our model achieves the best performance in terms of  $F_\beta$ ,  $E_\phi$ , and  $S_\alpha$  metrics. Except for  $E_\phi$  and  $MAE$ , the proposed method outperforms other SOTA models on the super-class “Amphibian”.

3) *Qualitative Evaluation:* Fig. 3 shows the qualitative comparison results. These examples are collected from five super-classes in the COD10K dataset, including “Aquatic”, “Terrestrial”, “Flying”, and “Amphibian”, and “Others” (from 1<sup>st</sup> row to 5<sup>th</sup> row). The challenge factors are also presented, *i.e.*, multiple objects (see the 6<sup>th</sup> and 7<sup>th</sup> rows) and occlusion (see the 8<sup>th</sup> and 9<sup>th</sup> rows). As shown in Fig. 3, C<sup>2</sup>F-Net improves the visual results compared to other COD methods in the detailed branches of the ghost pipefish and mantis (see the 1<sup>st</sup> and 3<sup>rd</sup> rows). In the context under different lightning, compared with PFNet [43], LSR [40], and SINet [15], our model can accurately identify camouflaged objects and their boundary (see the 5<sup>th</sup> row). For multiple objects, compared with PFNet [43], LSR [40], C<sup>2</sup>F-Net effectively detect multiple concealed objects (see the 6<sup>th</sup> and 7<sup>th</sup> rows). To detect occluded objects, compared with other methods, our

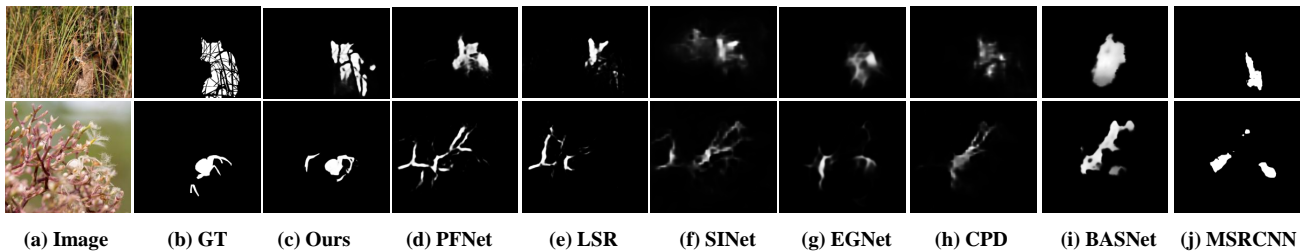


Fig. 4. Some failure cases of our model and seven comparison methods.



TABLE III  
ABLATION STUDIES ON THE THREE DATASETS. BEST RESULTS ARE HIGHLIGHTED IN **BOLD**. VER. = VERSION.

Ver.	Method	CAMO-Test					CHAMELEON					COD10K-Test				
		$S_\alpha \uparrow$	$E_\phi \uparrow$	$F_\beta^w \uparrow$	$F_\beta \uparrow$	$M \downarrow$	$S_\alpha \uparrow$	$E_\phi \uparrow$	$F_\beta^w \uparrow$	$F_\beta \uparrow$	$M \downarrow$	$S_\alpha \uparrow$	$E_\phi \uparrow$	$F_\beta^w \uparrow$	$F_\beta \uparrow$	$M \downarrow$
No.1	Basic	0.773	0.843	0.684	0.742	0.090	0.883	0.923	0.813	0.823	0.033	0.805	0.870	0.678	0.683	0.038
No.2	Basic+ACFM	0.784	0.852	0.699	0.751	0.087	0.885	0.932	0.821	0.829	0.032	0.810	0.881	0.678	0.697	<b>0.036</b>
No.3	Basic+DGCM	0.786	0.856	0.696	0.752	0.081	0.883	0.940	0.820	0.834	0.030	0.808	0.881	0.676	0.695	0.037
No.4	Basic+CIM	0.787	0.857	0.700	0.747	0.086	0.885	0.929	0.820	0.827	0.032	0.805	0.873	0.669	0.684	0.038
No.5	Basic+ACFM+DGCM	0.796	0.864	0.719	0.764	0.080	0.888	0.932	0.828	<b>0.844</b>	0.032	<b>0.813</b>	0.886	0.686	0.703	<b>0.036</b>
No.6	MSCA $\rightarrow$ Conv	0.785	0.852	0.700	0.748	0.084	0.888	0.935	0.826	0.835	0.031	0.810	0.873	0.679	0.693	0.037
No.7	Basic+ACFM+DGCM+CIM	<b>0.800</b>	<b>0.869</b>	<b>0.730</b>	<b>0.777</b>	<b>0.077</b>	<b>0.893</b>	<b>0.947</b>	<b>0.845</b>	0.836	<b>0.028</b>	0.811	<b>0.891</b>	<b>0.691</b>	<b>0.718</b>	<b>0.036</b>

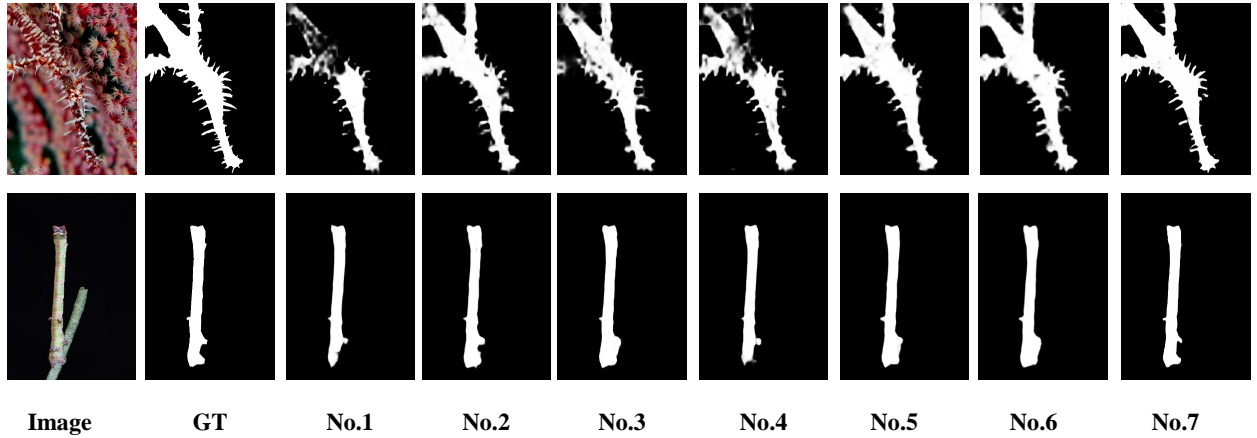


Fig. 5. Visual comparisons for showing the benefits of different modules. The results of No.1~No.7 are shown in Table III.

model can recognize the certain boundaries of the camouflaged objects. Overall, compared with other SOTA models, our C<sup>2</sup>F-Net can achieve better performance by detecting more accurate and complete camouflaged objects with rich details.

4) *Model Size and Inference Time*: The results, shown in Tables IV, are the model sizes and inference times of our model and representative models. # Param is measured in million (M) and memory is measured in giga (G). As can be observed, our model is with the minimal parameters in comparison with the representative models. Its memory cost is also controlled well, *i.e.*, much less than ERRNet and PFNet. However, we realize that the inference speed of our C<sup>2</sup>F-Net is not promising enough, which is mainly caused by the new improvement applied to our model. Specifically, the IJCAI version of our model can achieve an Fps of 39.07, which is reduced to 27.41 after using the CIM. We will seek to improve the CIM with more efficient design in future work. Note that we perform experiments to test the inference time on a single Tesla P100 GPU.

5) *Failure Cases*: We present a number of typical failure cases in Fig. 4. As can be observed, our model may fail in some extremely challenging cases. However, it is worth noting that, in these cases, existing SOTA models also fail and our model still outperforms the SOTA models.

TABLE IV  
COMPARISON OF MODEL SIZE AND INFERENCE TIME.

Method	# Param (M)	Memory (G)	Speed (Fps)
SINet [15]	48.946	19.475	30.85
PraNet [17]	30.498	13.078	42.60
LSR [40]	28.720	17.423	37.96
PFNet [43]	18.977	46.498	38.84
ERRNet [31]	67.708	40.050	53.34
C <sup>2</sup> F-Net	18.063	25.214	27.41

#### E. Ablation Study

To evaluate the effectiveness of each component in the proposed model, we designed seven ablation experiments (as presented in Table III). In the No.1 (Basic) experiment, we removed all ACFMs, DGCMs, and CIM, while keeping RFBs. The features from RFBs are added for predicting the COD result. In the No.2 (Basic+ACFM) experiment, we directly connected the two ACFMs by removing DGCMs and CIM. In the No.3 (Basic+DGCM) experiment, we replaced ACFMs with the combined operation of upsampling and then conducted an addition operation, while DGCMs keeping unchanged and CIM was removed. In the No.4 (Basic+CIM) experiment, we refined the features and then predicted the COD result with our CIM. In the No.5 (Basic+ACFM+DGCM) experiment, ACFMs and DGCMs are kept, while the CIM is taken out. In the No.6 (MSCA  $\rightarrow$  Conv) experiment, we

TABLE V  
QUANTITATIVE EVALUATION FOR POLYP SEGMENTATION ON THE FOUR DATASETS. THE BEST RESULTS ARE HIGHLIGHTED IN **BOLD** FONTS.

Method	CVC-300					CVC-ClinicDB					CVC-ColonDB					ETIS-LaribPolupDB				
	$S_\alpha \uparrow$	$E_\phi \uparrow$	$F_\beta^w \uparrow$	$F_\beta \uparrow$	$M \downarrow$	$S_\alpha \uparrow$	$E_\phi \uparrow$	$F_\beta^w \uparrow$	$F_\beta \uparrow$	$M \downarrow$	$S_\alpha \uparrow$	$E_\phi \uparrow$	$F_\beta^w \uparrow$	$F_\beta \uparrow$	$M \downarrow$	$S_\alpha \uparrow$	$E_\phi \uparrow$	$F_\beta^w \uparrow$	$F_\beta \uparrow$	$M \downarrow$
UNet [48]	0.843	0.867	0.684	0.703	0.022	0.889	0.917	0.811	0.804	0.019	0.712	0.763	0.498	0.569	0.061	0.684	0.645	0.366	0.398	0.036
UNet++ [68]	0.839	0.884	0.687	0.706	0.018	0.873	0.898	0.785	0.784	0.022	0.691	0.762	0.467	0.560	0.064	0.683	0.704	0.390	0.465	0.035
SFA [21]	0.640	0.604	0.341	0.353	0.065	0.793	0.816	0.647	0.655	0.042	0.634	0.648	0.379	0.407	0.094	0.557	0.515	0.231	0.255	0.109
PraNet [17]	0.925	0.938	0.843	0.824	0.010	0.936	0.957	0.896	0.885	<b>0.009</b>	0.820	0.847	0.699	0.718	<b>0.043</b>	0.794	0.792	0.600	0.602	<b>0.031</b>
C <sup>2</sup> F-Net	<b>0.928</b>	<b>0.970</b>	<b>0.864</b>	<b>0.868</b>	<b>0.008</b>	<b>0.942</b>	<b>0.978</b>	<b>0.923</b>	<b>0.922</b>	<b>0.009</b>	<b>0.821</b>	<b>0.883</b>	<b>0.713</b>	<b>0.735</b>	0.044	<b>0.798</b>	<b>0.853</b>	<b>0.629</b>	<b>0.649</b>	0.032

replaced MSCA with a convolutional block. Finally, No.7 (Basic+ACFM+DGCM+CIM) is the full version of our CIM.

**Effectiveness of ACFM.** We first study the effectiveness of ACFM. As shown in Table III, it can be observed that No.2 (Basic+ACFM) outperforms No.1 (Basic), clearly indicating that the ACFM is helpful and critical to boost the COD performance, increasing the  $F_\beta^w$  by 2.15% on CAMO. Compared to the basic network, the ACFM could improve the ability to detect the main part of the camouflaged object (4<sup>th</sup> col).

**Effectiveness of DGCM.** From the results in Table III, it can be seen that No.3 (Basic + DGCM) outperforms better than No.1 (Basic) on the all used datasets. Specifically, the adaptive  $E_\phi$  increased 1.81% on CHAMELEON. The results indicate that introducing the DGCM can enable our model to detect objects accurately.

**Effectiveness of CIM.** As shown in Table III, No.4 (Basic + CIM) outperforms No.1 (Basic) on three benchmarks datasets. This owes to CIM’s ability of exploiting multi-scale information from low-level features, which plays a crucial role in boosting the COD performance.

**Effectiveness of ACFM & DGCM.** To evaluate the combination of ACFM and DGCM, we carry out the ablation study of No.5. As shown in Table III, the performance of

the combination is generally better than the first four settings.

**Effectiveness of MSCA.** In this ablation study, we replace it with a convolutional layer (denoted “MSCA→Conv”). The comparison results of the No.6 are shown in Table III, indicating that the use of MSCA significantly improves the results, especially on the CAMO-Test dataset.

**Effectiveness of CIM & ACFM & DGCM.** To evaluate the full version of our model, we test the performance of No.7. From the results in Table III, it can be seen that the full version of C<sup>2</sup>F-Net is better than all other ablated ones. Additionally, the visual comparisons in Fig. 5 further show that our full model is more conducive to identifying and locating camouflaged objects.

It is worth noting that No.5 (Basic+ACFM+DGCM) is the conference version of our model, which was published in IJCAI 2021 [52]. The results, shown in Table I, indicate that the full version of our C<sup>2</sup>F-Net (*i.e.*, No.7) outperforms No. 5 on all three datasets. This sufficiently demonstrates the effectiveness of our new improvement applied to the model. The underlying reason for effectiveness lies in the ability of CIM in exploiting useful information from low-level features with the guidance of coarse prediction map. In addition, the MRBs in CIM promote making full use of the features

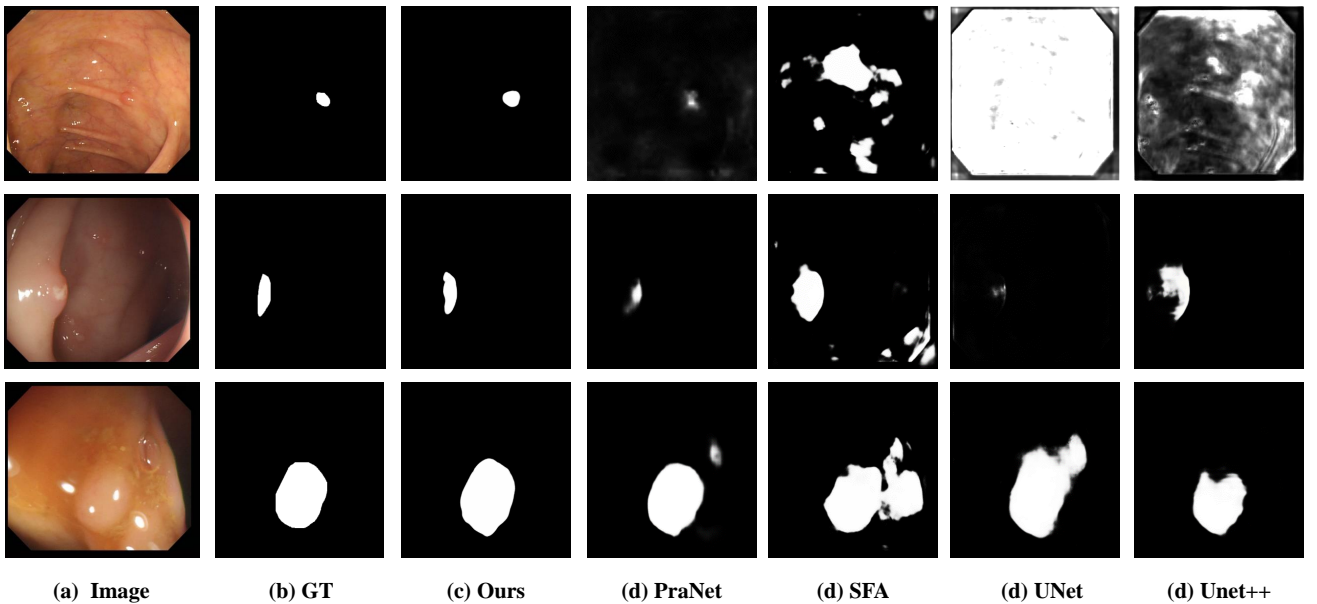


Fig. 6. Visual comparisons of different methods on the polyp segmentation task.

for improved performance. Due to these novel designs, CIM effectively improves the performance and provides results much better than the previous version [52].

#### F. Application to Polyp Segmentation

As aforementioned in Sec. II-C, COD has rich downstream applications in practice. Therefore, we further evaluate our C<sup>2</sup>F-Net by applying it to a typical COD downstream application, polyp segmentation.

Experiments are conducted on four public datasets, including ETIS [51], CVC-ClinicCB [2], CVC-ColonDB [53], and CVC-300 [55]. We compare C<sup>2</sup>F-Net with four cutting-edge polyp segmentation models, *i.e.*, UNet [48], UNet++ [68], SFA [21], and PraNet [17]. The results of these four methods are taken from <https://github.mscom/DengPingFan/PraNet>. Similar to the COD experiments, we evaluate the results using five metrics, including MAE,  $S_\alpha$ ,  $F_\beta^w$ ,  $F_\beta$ , and  $E_\phi$ .

1) *Qualitative Evaluation*: Table V summarizes the quantitative results of different methods on four polyp datasets.

**Performance on CVC-300.** As shown in Table V, C<sup>2</sup>F-Net outperforms the other four cutting-edge methods on CVC-300. Compared with the second-best method, ParNet [17], the performance of  $E_\phi$  improves by 3.30%.

**Performance on CVC-ClinicDB.** We further test our model on CVC-ClinicDB, which includes 612 open-access images from 31 colonoscopy clips. The performance of  $F_\beta$  increases by 4.01%.

**Performance on CVC-ColonDB.** CVC-ColonDB is a small dataset, which contains 380 images from 15 short colons copy sequences. Except for the MAE, C<sup>2</sup>F-Net obtains better performance. Especially, compared to ParNet [17], the performance of  $E_\phi$  increases by 4.01%.

**Performance on ETIS.** ETIS consists of 196 polyp images for early diagnosis of colorectal cancer. Compared to ParNet [17], the results of  $E_\phi$  and  $F_\beta$  are increased by 7.15% and 7.24%, respectively.

2) *Qualitative Evaluation*: Fig. 6 shows the visual results of different models on four polyp datasets, including small polyps (1<sup>st</sup> row), different lightning (2<sup>nd</sup> row), and low-contrast scenes (3<sup>rd</sup> row). For the small polyps, C<sup>2</sup>F-Net can accurately detect boundaries, while UNet [48] and UNet++ [68] fail. Furthermore, our model outperforms competing methods under different lightning (2<sup>nd</sup> row), demonstrating its ability to identify polyps under poor visual conditions. In the condition of low-contrast scenes, the results of C<sup>2</sup>F-Net make the minimum error areas (3<sup>rd</sup> row). We can see that C<sup>2</sup>F-Net performs better than PraNet [17], the SOTA poly segmentation model that is designed to handle challenging conditions, such as varied size, complicated context, and so on.

#### V. CONCLUSION

In this paper, we have proposed a novel C<sup>2</sup>F-Net for the COD task. Our C<sup>2</sup>F-Net can effectively integrate the cross-level features that contain rich global context information. In C<sup>2</sup>F-Net, DGCMS are proposed to exploit global context information from the fused features. Furthermore, the high-level features are fused with ACFMs, which integrate the

features under the guidance of valuable attention cues provided by MSCAs. Finally, we propose CIM to predict the final result from the low-level features enhanced by the coarse prediction map. Experiments on three public datasets show that our model outperforms other state-of-the-art COD methods. Moreover, the ablation studies validate the effectiveness of each key component. Further evaluation on the four polyp segmentation datasets demonstrates the promising potentials of our C<sup>2</sup>F-Net in COD downstream applications.

#### ACKNOWLEDGMENT

This work was supported in part by the National Science Fund of China under Grant 62172228, an Open Project of the Key Laboratory of System Control and Information Processing, Ministry of Education (Shanghai Jiao Tong University, ID: Scip202102), and the Fundamental Research Funds for the Central Universities (Grant No. D5000220213).

#### REFERENCES

- [1] M. Akbari, M. Mohrekeh, E. Nasr-Esfahani, S. R. Soroushmehr, N. Karimi, S. Samavi, and K. Najarian, "Polyp segmentation in colonoscopy images using fully convolutional network," in *2018 40th Annual International Conference of the IEEE Engineering in Medicine and Biology Society*. IEEE, 2018, pp. 69–72.
- [2] J. Bernal, F. J. Sánchez, G. Fernández-Esparrach, D. Gil, C. Rodríguez, and F. Vilariño, "Wm-dova maps for accurate polyp highlighting in colonoscopy: Validation vs. saliency maps from physicians," *Computerized Medical Imaging and Graphics*, vol. 43, pp. 99–111, 2015.
- [3] H. Bi, C. Zhang, K. Wang, J. Tong, and F. Zheng, "Rethinking camouflaged object detection: Models and datasets," *IEEE Transactions on Circuits and Systems for Video Technology*, 2021.
- [4] P. Brandao, E. Mazomenos, G. Ciuti, R. Calì, F. Bianchi, A. Menciassi, P. Dario, A. Koulouzidis, A. Arezzo, and D. Stoyanov, "Fully convolutional neural networks for polyp segmentation in colonoscopy," in *Medical Imaging 2017: Computer-Aided Diagnosis*, vol. 10134. International Society for Optics and Photonics, 2017, p. 101340F.
- [5] K. Chen, J. Pang, J. Wang, Y. Xiong, X. Li, S. Sun, W. Feng, Z. Liu, J. Shi, W. Ouyang *et al.*, "Hybrid task cascade for instance segmentation," in *Proceedings of the IEEE/CVF Conference on Computer Vision and Pattern Recognition*, 2019, pp. 4974–4983.
- [6] L.-C. Chen, G. Papandreou, I. Kokkinos, K. Murphy, and A. L. Yuille, "DeepLab: Semantic image segmentation with deep convolutional nets, atrous convolution, and fully connected crfs," *IEEE Transactions on Pattern Analysis and Machine Intelligence*, vol. 40, no. 4, pp. 834–848, 2017.
- [7] Z. Chen, R. Cong, Q. Xu, and Q. Huang, "Dpanet: Depth potentiality-aware gated attention network for rgb-d salient object detection," *IEEE Transactions on Image Processing*, vol. 30, pp. 7012–7024, 2020.
- [8] Z. Chen, Q. Xu, R. Cong, and Q. Huang, "Global context-aware progressive aggregation network for salient object detection," in *Proceedings of the AAAI Conference on Artificial Intelligence*, vol. 34, no. 07, 2020, pp. 10599–10606.
- [9] R. Cong, J. Lei, H. Fu, W. Lin, Q. Huang, X. Cao, and C. Hou, "An iterative co-saliency framework for rgbd images," *IEEE transactions on cybernetics*, vol. 49, no. 1, pp. 233–246, 2017.
- [10] R. Cong, Y. Zhang, L. Fang, J. Li, C. Zhang, Y. Zhao, and S. Kwong, "Rmet: Relational reasoning network with parallel multi-scale attention for salient object detection in optical remote sensing images," *IEEE Transactions on Geoscience and Remote Sensing*, 2021.
- [11] Y. Dai, F. Giesecke, S. Oehmcke, Y. Wu, and K. Barnard, "Attentional feature fusion," in *Proceedings of the IEEE/CVF Winter Conference on Applications of Computer Vision*, 2021, pp. 3560–3569.
- [12] D.-P. Fan, M.-M. Cheng, Y. Liu, T. Li, and A. Borji, "Structure-measure: A new way to evaluate foreground maps," in *Proceedings of the IEEE International Conference on Computer Vision*, 2017, pp. 4548–4557.
- [13] D.-P. Fan, C. Gong, Y. Cao, B. Ren, M.-M. Cheng, and A. Borji, "Enhanced-alignment measure for binary foreground map evaluation," in *International Joint Conference on Artificial Intelligence*, 2018.

- [14] D.-P. Fan, G.-P. Ji, X. Qin, and M.-M. Cheng, "Cognitive vision inspired object segmentation metric and loss function," *SCIENTIA SINICA Informationis*, vol. 6, 2021.
- [15] D.-P. Fan, G.-P. Ji, G. Sun, M.-M. Cheng, J. Shen, and L. Shao, "Camouflaged object detection," in *Proceedings of the IEEE/CVF Conference on Computer Vision and Pattern Recognition*, 2020, pp. 2777–2787.
- [16] —, "Concealed object detection," *IEEE Transactions on Pattern Analysis and Machine Intelligence*, 2021.
- [17] D.-P. Fan, G.-P. Ji, T. Zhou, G. Chen, H. Fu, J. Shen, and L. Shao, "Pranet: Parallel reverse attention network for polyp segmentation," in *International Conference on Medical Image Computing and Computer-Assisted Intervention*. Springer, 2020, pp. 263–273.
- [18] D.-P. Fan, T. Li, Z. Lin, G.-P. Ji, D. Zhang, M.-M. Cheng, H. Fu, and J. Shen, "Re-thinking co-salient object detection," *IEEE TPAMI*, 2021.
- [19] D.-P. Fan, Y. Zhai, A. Borji, J. Yang, and L. Shao, "BBS-Net: RGB-D salient object detection with a bifurcated backbone strategy network," in *European Conference on Computer Vision*. Springer, 2020, pp. 275–292.
- [20] D.-P. Fan, T. Zhou, G.-P. Ji, Y. Zhou, G. Chen, H. Fu, J. Shen, and L. Shao, "Inf-net: Automatic covid-19 lung infection segmentation from ct images," *IEEE TMI*, vol. 39, no. 8, pp. 2626–2637, 2020.
- [21] Y. Fang, C. Chen, Y. Yuan, and K.-y. Tong, "Selective feature aggregation network with area-boundary constraints for polyp segmentation," in *International Conference on Medical Image Computing and Computer-Assisted Intervention*. Springer, 2019, pp. 302–310.
- [22] J. Fu, J. Liu, H. Tian, Y. Li, Y. Bao, Z. Fang, and H. Lu, "Dual attention network for scene segmentation," in *Proceedings of the IEEE/CVF Conference on Computer Vision and Pattern Recognition*, 2019, pp. 3146–3154.
- [23] S. Gao, M.-M. Cheng, K. Zhao, X.-Y. Zhang, M.-H. Yang, and P. H. Torr, "Res2net: A new multi-scale backbone architecture," *IEEE transactions on pattern analysis and machine intelligence*, 2019.
- [24] K. He, G. Gkioxari, P. Dollár, and R. Girshick, "Mask r-cnn," in *Proceedings of the IEEE International Conference on Computer Vision*, 2017, pp. 2961–2969.
- [25] N. Huang, Y. Yang, D. Zhang, Q. Zhang, and J. Han, "Employing bilinear fusion and saliency prior information for rgb-d salient object detection," *IEEE Transactions on Multimedia*, 2021.
- [26] Z. Huang, L. Huang, Y. Gong, C. Huang, and X. Wang, "Mask scoring r-cnn," in *Proceedings of the IEEE/CVF Conference on Computer Vision and Pattern Recognition*, 2019, pp. 6409–6418.
- [27] Z. Huang, X. Wang, L. Huang, C. Huang, Y. Wei, and W. Liu, "Ccnet: Criss-cross attention for semantic segmentation," in *Proceedings of the IEEE/CVF International Conference on Computer Vision*, 2019, pp. 603–612.
- [28] D. Jha, P. H. Smedsrud, M. A. Riegler, D. Johansen, T. De Lange, P. Halvorsen, and H. D. Johansen, "Resunet++: An advanced architecture for medical image segmentation," in *2019 IEEE International Symposium on Multimedia (ISM)*. IEEE, 2019, pp. 225–2255.
- [29] G.-P. Ji, Y.-C. Chou, D.-P. Fan, G. Chen, D. Jha, H. Fu, and L. Shao, "Progressively normalized self-attention network for video polyp segmentation," in *MICCAI*, 2021, pp. 142–152.
- [30] G.-P. Ji, G. Xiao, Y.-C. Chou, D.-P. Fan, K. Zhao, G. Chen, H. Fu, and L. Van Gool, "Deep learning for video polyp segmentation: A comprehensive study," *arXiv*, 2022.
- [31] G.-P. Ji, L. Zhu, M. Zhuge, and K. Fu, "Fast camouflaged object detection via edge-based reversible re-calibration network," *Pattern Recognition*, p. 108414, 2021.
- [32] Z. Jiang, "Object modelling and tracking in videos via multidimensional features," *International Scholarly Research Notices*, vol. 2011, 2011.
- [33] H. Lamdouar, C. Yang, W. Xie, and A. Zisserman, "Betrayed by motion: Camouflaged object discovery via motion segmentation," in *Proceedings of the Asian Conference on Computer Vision*, 2020.
- [34] T.-N. Le, T. V. Nguyen, Z. Nie, M.-T. Tran, and A. Sugimoto, "Anabran network for camouflaged object segmentation," *Computer Vision and Image Understanding*, vol. 184, pp. 45–56, 2019.
- [35] A. Li, J. Zhang, Y. Lv, B. Liu, T. Zhang, and Y. Dai, "Uncertainty-aware joint salient object and camouflaged object detection," in *Proceedings of the IEEE/CVF Conference on Computer Vision and Pattern Recognition*, 2021, pp. 10071–10081.
- [36] W. Li, Z. Zhang, X. Wang, and P. Luo, "Adax: Adaptive gradient descent with exponential long term memory," *arXiv preprint arXiv:2004.09740*, 2020.
- [37] T.-Y. Lin, P. Dollár, R. Girshick, K. He, B. Hariharan, and S. Belongie, "Feature pyramid networks for object detection," in *Proceedings of the IEEE Conference on Computer Vision and Pattern Recognition*, 2017, pp. 2117–2125.
- [38] J.-J. Liu, Q. Hou, M.-M. Cheng, J. Feng, and J. Jiang, "A simple pooling-based design for real-time salient object detection," in *Proceedings of the IEEE/CVF Conference on Computer Vision and Pattern Recognition*, 2019, pp. 3917–3926.
- [39] N. Liu, J. Han, and M.-H. Yang, "Picanet: Learning pixel-wise contextual attention for saliency detection," in *Proceedings of the IEEE Conference on Computer Vision and Pattern Recognition*, 2018, pp. 3089–3098.
- [40] Y. Lv, J. Zhang, Y. Dai, A. Li, B. Liu, N. Barnes, and D.-P. Fan, "Simultaneously localize, segment and rank the camouflaged objects," in *Proceedings of the IEEE/CVF Conference on Computer Vision and Pattern Recognition*, 2021, pp. 11591–11601.
- [41] A. V. Mamonov, I. N. Figueiredo, P. N. Figueiredo, and Y.-H. R. Tsai, "Automated polyp detection in colon capsule endoscopy," *IEEE transactions on medical imaging*, vol. 33, no. 7, pp. 1488–1502, 2014.
- [42] R. Margolin, L. Zelnik-Manor, and A. Tal, "How to evaluate foreground maps?" in *Proceedings of the IEEE conference on Computer Vision and Pattern Recognition*, 2014, pp. 248–255.
- [43] H. Mei, G.-P. Ji, Z. Wei, X. Yang, X. Wei, and D.-P. Fan, "Camouflaged object segmentation with distraction mining," in *Proceedings of the IEEE/CVF Conference on Computer Vision and Pattern Recognition*, 2021, pp. 8772–8781.
- [44] A. Mondal, "Camouflaged object detection and tracking: A survey," *International Journal of Image and Graphics*, vol. 20, no. 04, p. 2050028, 2020.
- [45] B. Murugesan, K. Sarveswaran, S. M. Shankaranarayana, K. Ram, J. Joseph, and M. Sivaprakasam, "Psi-net: Shape and boundary aware joint multi-task deep network for medical image segmentation," in *2019 41st Annual International Conference of the IEEE Engineering in Medicine and Biology Society (EMBC)*. IEEE, 2019, pp. 7223–7226.
- [46] X. Qin, Z. Zhang, C. Huang, C. Gao, M. Dehghan, and M. Jagersand, "Basnet: Boundary-aware salient object detection," in *Proceedings of the IEEE/CVF Conference on Computer Vision and Pattern Recognition*, 2019, pp. 7479–7489.
- [47] J. Ren, X. Hu, L. Zhu, X. Xu, Y. Xu, W. Wang, Z. Deng, and P.-A. Heng, "Deep texture-aware features for camouflaged object detection," *IEEE Transactions on Circuits and Systems for Video Technology*, 2021.
- [48] O. Ronneberger, P. Fischer, and T. Brox, "U-Net: Convolutional networks for biomedical image segmentation," in *MICCAI*, 2015, pp. 234–241.
- [49] X. Shu, J. Yang, R. Yan, and Y. Song, "Expansion-squeeze-excitation fusion network for elderly activity recognition," *IEEE Transactions on Circuits and Systems for Video Technology*, 2022.
- [50] X. Shu, L. Zhang, G.-J. Qi, W. Liu, and J. Tang, "Spatiotemporal co-attention recurrent neural networks for human-skeleton motion prediction," *IEEE Transactions on Pattern Analysis and Machine Intelligence*, 2021.
- [51] J. Silva, A. Histace, O. Romain, X. Dray, and B. Granado, "Toward embedded detection of polyps in wce images for early diagnosis of colorectal cancer," *International Journal of Computer Assisted Radiology and Surgery*, vol. 9, no. 2, pp. 283–293, 2014.
- [52] Y. Sun, G. Chen, T. Zhou, Y. Zhang, and N. Liu, "Context-aware cross-level fusion network for camouflaged object detection," in *International Joint Conference on Artificial Intelligence*, 2021.
- [53] N. Tajbakhsh, S. R. Gurudu, and J. Liang, "Automatic polyp detection in colonoscopy videos using an ensemble of convolutional neural networks," in *2015 IEEE 12th International Symposium on Biomedical Imaging (ISBI)*. IEEE, 2015, pp. 79–83.
- [54] J. Tan, P. Xiong, Z. Lv, K. Xiao, and Y. He, "Local context attention for salient object segmentation," in *Proceedings of the Asian Conference on Computer Vision*, 2020.
- [55] D. Vázquez, J. Bernal, F. J. Sánchez, G. Fernández-Esparrach, A. M. López, A. Romero, M. Drozdal, and A. Courville, "A benchmark for endoluminal scene segmentation of colonoscopy images," *Journal of Healthcare Engineering*, vol. 2017, 2017.
- [56] X. Wang, R. Girshick, A. Gupta, and K. He, "Non-local neural networks," in *Proceedings of the IEEE conference on Computer Vision and Pattern Recognition*, 2018, pp. 7794–7803.
- [57] J. Wei, S. Wang, and Q. Huang, "F<sup>3</sup>net: Fusion, feedback and focus for salient object detection," in *Proceedings of the AAAI Conference on Artificial Intelligence*, vol. 34, no. 07, 2020, pp. 12321–12328.
- [58] Y.-H. Wu, Y. Liu, L. Zhang, W. Gao, and M.-M. Cheng, "Regularized densely-connected pyramid network for salient instance segmentation," *IEEE Transactions on Image Processing*, vol. 30, pp. 3897–3907, 2021.
- [59] Z. Wu, L. Su, and Q. Huang, "Cascaded partial decoder for fast and accurate salient object detection," in *Proceedings of the IEEE/CVF*

*Conference on Computer Vision and Pattern Recognition*, 2019, pp. 3907–3916.

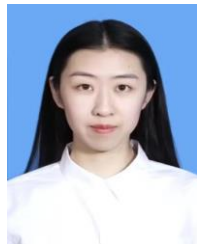
- [60] J. Yan, T.-N. Le, K.-D. Nguyen, M.-T. Tran, T.-T. Do, and T. V. Nguyen, “Mirrornet: Bio-inspired adversarial attack for camouflaged object segmentation,” *arXiv e-prints*, pp. arXiv–2007, 2020.
- [61] L. Zhang, J. Dai, H. Lu, Y. He, and G. Wang, “A bi-directional message passing model for salient object detection,” in *Proceedings of the IEEE Conference on Computer Vision and Pattern Recognition*, 2018, pp. 1741–1750.
- [62] Q. Zhang, N. Huang, L. Yao, D. Zhang, C. Shan, and J. Han, “Rgb-t salient object detection via fusing multi-level cnn features,” *IEEE Transactions on Image Processing*, vol. 29, pp. 3321–3335, 2019.
- [63] Q. Zhang, R. Cong, C. Li, M.-M. Cheng, Y. Fang, X. Cao, Y. Zhao, and S. Kwong, “Dense attention fluid network for salient object detection in optical remote sensing images,” *IEEE Transactions on Image Processing*, vol. 30, pp. 1305–1317, 2020.
- [64] X. Zhang, C. Zhu, S. Wang, Y. Liu, and M. Ye, “A bayesian approach to camouflaged moving object detection,” *IEEE Transactions on Circuits and Systems for Video Technology*, vol. 27, no. 9, pp. 2001–2013, 2017.
- [65] H. Zhao, J. Shi, X. Qi, X. Wang, and J. Jia, “Pyramid scene parsing network,” in *Proceedings of the IEEE conference on computer vision and pattern recognition*, 2017, pp. 2881–2890.
- [66] J.-X. Zhao, J.-J. Liu, D.-P. Fan, Y. Cao, J. Yang, and M.-M. Cheng, “Egnet: Edge guidance network for salient object detection,” in *Proceedings of the IEEE/CVF International Conference on Computer Vision*, 2019, pp. 8779–8788.
- [67] T. Zhao and X. Wu, “Pyramid feature attention network for saliency detection,” in *Proceedings of the IEEE/CVF Conference on Computer Vision and Pattern Recognition*, 2019, pp. 3085–3094.
- [68] Z. Zhou, M. M. R. Siddiquee, N. Tajbakhsh, and J. Liang, “Unet++: Redesigning skip connections to exploit multiscale features in image segmentation,” *IEEE Transactions on Medical Imaging*, vol. 39, no. 6, pp. 1856–1867, 2019.
- [69] M. Zhuge, X. Lu, Y. Guo, Z. Cai, and S. Chen, “Cubenet: X-shape connection for camouflaged object detection,” *Pattern Recognition*, p. 108644, 2022.



**Geng Chen** is a Professor at Northwestern Polytechnical University, China. He received his Ph.D. from Northwestern Polytechnical University, China, in 2016. He was a research scientist at the Inception Institute of Artificial Intelligence, UAE, from 2019 to 2021, and a postdoctoral research associate at the University of North Carolina at Chapel Hill, USA, from 2016 to 2019. His research interests lie in medical image analysis and computer vision.



**Si-Jie Liu** is currently a Ph.D. student with School of Power and Energy, Northwestern Polytechnical University, China, under the supervision of Prof Ya-Feng Wu. His research interests mainly focus on computer measurement & control, digital twin for industrial equipment maintenance, and computer vision.



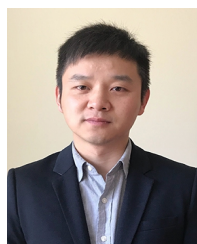
**Yu-Jia Sun** is currently a master student with School of Computer Science, Inner Mongolia university, China, under the supervision of Prof Hong-Xi Wei. Her research interests mainly focus on computer vision and camouflaged object detection.



**Ge-Peng Ji** is currently a master student of Communication and Information System at School of Computer Science, Wuhan University. His research interests lie in designing deep neural networks and applying deep learning in various fields of lowlevel vision, such as RGB salient object detection, RGB-D salient object detection, video object segmentation, concealed object detection, and medical image segmentation.



**Ya-Feng Wu** is a Professor with School of Power and Energy, Northwestern Polytechnical University, China. He received his Ph.D. from Northwestern Polytechnical University, China, in 2002. His main research interests include modern signal processing, active noise control, and computer measurement & control.



**Tao Zhou** received the Ph.D. degree in Pattern Recognition and Intelligent Systems from the Institute of Image Processing and Pattern Recognition, Shanghai Jiao Tong University, in 2016. From 2016 to 2018, he was a Postdoctoral Fellow in the BRIC and IDEA lab, University of North Carolina at Chapel Hill. From 2018 to 2020, he was a Research Scientist at the Inception Institute of Artificial Intelligence (IIAI), Abu Dhabi. He is currently a Professor in the School of Computer Science and Engineering, Nanjing University of Science and Technology, China. His research interests include machine learning, computer vision, and medical image analysis.